




Article

Doping Zinc Oxide Nanoparticles by Magnetic and Nonmagnetic Nanocomposites Using Organic Species for Fast Removal of Industrial Pollutants from Water in UV Light

Osama Saber ^{1,2,3,*} , Mostafa Osama ^{1,2}, Nagih M. Shaalan ^{1,2,4} , Aya Osama ^{1,2}, Adil Alshoaibi ^{1,2}  and Doaa Osama ^{1,2}

- ¹ Al Bilad Bank Scholarly Chair for Food Security in Saudi Arabia, The Deanship of Scientific Research, The Vice Presidency for Graduate Studies and Scientific Research, King Faisal University, P.O. Box 400, Al-Ahsa 31982, Saudi Arabia; 214110595@student.kfu.edu.sa (M.O.); nmohammed@kfu.edu.sa (N.M.S.); 217044956@student.kfu.edu.sa (A.O.); adshoaibi@kfu.edu.sa (A.A.); 221445253@student.kfu.edu.sa (D.O.)
² Department of Physics, College of Science, King Faisal University, P.O. Box 400, Al-Ahsa 31982, Saudi Arabia
³ Egyptian Petroleum Research Institute, Nasr City, P.O. Box 11727, Cairo 11765, Egypt
⁴ Physics Department, Faculty of Science, Assiut University, P.O. Box 71515, Assiut 71516, Egypt
* Correspondence: osmohamed@kfu.edu.sa; Tel.: +966-13-589-9440

Abstract: Advanced photo-active materials have attracted attention for their potential uses in water purification. In this study, a novel and facile route was used for designing nanohybrids to be valuable sources for producing effective photocatalysts for purifying water from the colored pollutants. Host-guest interaction and intercalation reactions used long chains of hydrocarbons of n-capric acid and stearic acid to facilitate incorporation of fine particles of cobalt iron oxide nanocomposite with the internal surface of the nanolayers of Al/Zn for building nanohybrids. The thermal decomposition of the prepared nanohybrids led to formation of zinc oxide nanoparticles doped with multi-oxides of magnetic and non-magnetic dopants. These dopants created new optical centers causing a strong reduction in the band gap energy from 3.30 eV to 2.60 eV. This positive effect was confirmed by a complete removal of the dye of Naphthol green B from water after 15 min of light irradiation. Moreover, a kinetic study showed that the reaction rate of photocatalytic degradation of the pollutants was faster than that of the conventional photocatalysts. Finally, this route was effective for producing benign and fast solutions for purifying water in addition to environment-related problems.

Keywords: magnetic doping; multi-oxides dopants; nanohybrids; nanolayers; photocatalytic degradation; purification of water



Citation: Saber, O.; Osama, M.; Shaalan, N.M.; Osama, A.; Alshoaibi, A.; Osama, D. Doping Zinc Oxide Nanoparticles by Magnetic and Nonmagnetic Nanocomposites Using Organic Species for Fast Removal of Industrial Pollutants from Water in UV Light. *Crystals* **2022**, *12*, 811. <https://doi.org/10.3390/cryst12060811>

Academic Editors: Assem Barakat, Ayman El-Faham, Saied Soliman and Stefano Carli

Received: 5 May 2022

Accepted: 31 May 2022

Published: 8 June 2022

Publisher's Note: MDPI stays neutral with regard to jurisdictional claims in published maps and institutional affiliations.



Copyright: © 2022 by the authors. Licensee MDPI, Basel, Switzerland. This article is an open access article distributed under the terms and conditions of the Creative Commons Attribution (CC BY) license (<https://creativecommons.org/licenses/by/4.0/>).

1. Introduction

Currently, the remediation of the environment and water-related problems is a goal for scientific communities around the world because of the rapidly growing population and industries. Most of the organic dyes such as textile dyes and surfactants are not easily biodegradable; therefore, they belong to colored hazardous pollutants. Photocatalytic degradation is a benign solution for purifying water from organic dyes using photocatalysts and light [1–3]. Semiconductor photo-catalysts are frequently used in this trend to solve environmental problems and purify wastewater [4–7]. Although, titanium oxide is one of the most famous photo-catalysts in this field, their applications are limited [8–10]. Therefore, zinc oxide is suggested to be an alternative photocatalyst to titanium oxide because it has large excitation binding energy of 60 meV in addition to band gap energy of 3.36 eV. According to the results of Dindar and Icli [11], zinc oxide was more effective than titanium oxide for the photocatalytic degradation of phenol. Many researchers confirmed this conclusion using zinc oxide and titanium oxide semiconductors for the advanced oxidation of wastewater [12,13]. However, low performance of zinc oxide was observed

for photocatalytic degradation in many studies [14–16] because of the high rate of the recombination reactions between the photo-generated electrons and holes of zinc oxides which happened within nanoseconds in addition to the low amount of energy absorbed in the photocatalytic processes. These disadvantages limit the potential capability of using this technique on a large scale.

Several techniques were used for modifying the structure of zinc oxide to solve its problems through narrowing its band gap energy to be more active and increase the absorbed quantum yield from light. The formation of nanostructures [17], combination with carbon nano-rods and nanotubes [18], and introducing surface defects were good solutions for improving the activity of zinc oxides. Moreover, for preventing the disadvantages of zinc oxide doping processes with transition elements in addition to morphological changes [19] were studied to be suitable solutions for increasing the performance of zinc oxide for photocatalytic degradation of pollutants. In this trend, the optical properties and activity of zinc oxide were developed through the morphological changes from nanoparticles [20] to nano-rods [21]. In addition, the zinc oxides nanotubes [22] and nanowires [23] were suggested to be active photocatalysts [24]. Different methods [25] were used for preparing zinc oxide such as sol-gel, spray pyrolysis, and solvent thermal.

Many researchers have used transition elements for doping zinc oxide to become effective photocatalysts [26–29]. Insertion of sulfur inside the structure of ZnO improved the charges separation by preventing the recombination process between electrons and holes [30]. The results of Adeel et al. showed high photocatalytic degradation of rhodamine blue and methylene blue under UV irradiation using ZnO films which modified by the addition of Ag and Al [31]. Introduction of nitrogen using the micro-emulsion method increased the optical properties and activity of ZnO nano-spheres [32]. In addition, several studies concluded that the addition of aluminum and iron as dopants inside ZnO structures converted their transparent thin films to be useful for photocatalytic applications and solar cells [33–38]. This positive effect of the addition of aluminum inside zinc oxide was confirmed by our previous research [7]. Thus, the current research aims to improve the photocatalytic activity of ZnO structure through building nanohybrids based on organic, magnetic, and inorganic species through an unconventional technique. In the conventional methods [39], multi-steps were used for mixing one or two elements for zinc oxides. However, it is difficult to obtain a homogenous distribution for all dopants in the matrix of ZnO in this way.

The nano-size spinel ferrite particles CoFe_2O_4 have recently received considerable attention because of their remarkable photocatalytic properties [40–43]. Although, research have been carried out for studying the photocatalytic performance of cobalt ferrite nanoparticles, there are no articles for using CoFe_2O_4 as filler for the zinc oxide structure. Furthermore, because of the low band gap energy of cobalt iron oxide CoFe_2O_4 (1.32 eV) [43], it is an excellent dopant and filler for reducing the band gap energy of zinc oxide.

Following this trend, the current study focuses on a non-conventional strategy for multi-doping zinc oxides through magnetic and nonmagnetic elements for the first time to reduce its band gap energy and to be effective for purifying water from colored pollutants. In this study, series of zinc oxides based on magnetic, inorganic, and organic species were prepared through building inorganic-magnetic-organic nanohybrids. Organic species, magnetic nanoparticles, and the nanolayers of zinc and aluminum oxides (or hydroxides) were used as pillars, fillers, and roofs to build the nanolayered structures of nanohybrids. Moreover, Al/Zn nanolayered structures were prepared without magnetic or organic species for comparison. These nanohybrids were used as sources for producing zinc oxide nanohybrids. Zinc oxide nanohybrids were tested for purifying the water through photocatalytic degradation of the colored pollutants. At the same time, the optical properties and activity of the nanohybrids were studied and compared with the conventional photocatalysts. In addition, a kinetic study was carried out to evaluate the activity of the prepared nanohybrids.

2. Materials and Methods

The hetero-structured hybrids such as inorganic-magnetic-organic systems are good candidates for creating unusual optical properties for zinc oxide, which cannot be achieved by conventional methods.

In order to build organic-inorganic-magnetic nanohybrids based on zinc oxide, three types of nanomaterials were prepared. Because of the low band gap energy of cobalt iron oxide CoFe_2O_4 (1.32 eV) [43], very fine nanoparticles of CoFe_2O_4 were prepared and used as filler for the nanohybrids and as dopant for reducing the band gap energy and increasing the photo activity of Zinc oxide. The second nanomaterial was nanolayered structures based on Al/Zn LDHs. The third type depended on the long chains of organic fatty acid to expand and widen the interlayered spacing of the nanolayered structures as shown in Figure 1. Two organic fatty acids were selected to build the nanohybrids. Stearic and n-capric acids have two advantages: They have long chains of aliphatic hydrocarbon (thin, long, and not bulky) that look similar to pillars that are easy to intercalate among the nanolayers and widen the interlayered spacing between the nanolayers. In addition, they have only one negative charge on one of their ends to attack and bond with the positive charge of the nanolayers as shown in Figure 1. This widening and expansion can facilitate the insertion of magnetic nanoparticles among the nanolayers of Al/Zn LDHs. To study the important role of organic fatty acid, two organic fatty acids were used to build two inorganic-magnetic-organic nanohybrids.

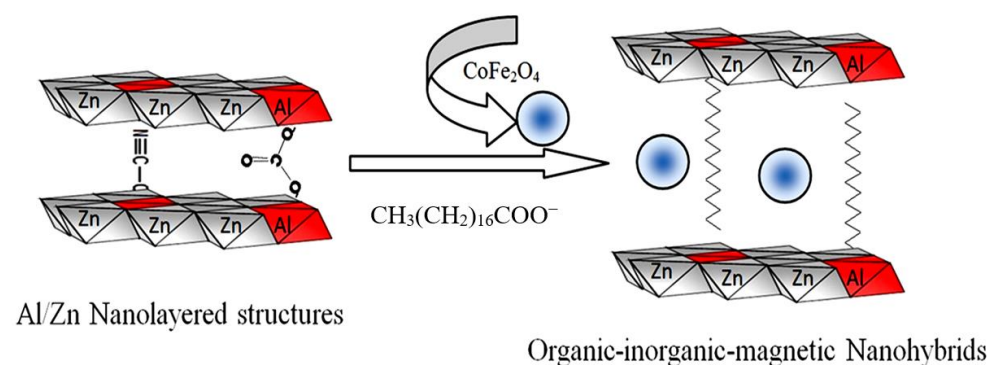


Figure 1. Schematic representation for building organic-inorganic-magnetic nanohybrids.

2.1. Preparation of Nanoparticles of Magnetic Nanocomposites

A solvent thermal technique [1,7] was used for preparing very fine nanoparticles of cobalt iron nanocomposite. Cobalt (II) acetate (0.051 mol) and Iron (II) acetate (0.026 mol) were reacted with 350 mL of methanol at room temperature for 5 h to produce Sol of methoxides. A similar amount of ethanol was added for the mixture. To complete the reaction under super critical conditions of pressure and temperature, the mixture was placed inside an autoclave. The mixture was heated at a slow rate, 1 °C /min to reach 260 °C under high pressure 75 bar. At this critical temperature, the Sol converted to Gel by poly-condensation or poly-esterification reactions that result in a dramatic increase in the viscosity of the solution during heating inside the autoclave. Poly-condensation reactions continued until the gel transformed into a solid mass of CoFe_2O_4 . At this stage, the pressure was slowly released under the flow of nitrogen to avoid oxidation reactions. At the same time, the temperature of the autoclave decreased to room temperature. The fine powder of the product was easily collected.

2.2. Preparation of Nanolayered Structures and Nanohybrids

Two samples of inorganic-magnetic-organic nanohybrids were prepared for designing a nanolayered structure changing the organic species [2,6]. A pure nanolayered structure of Al/Zn LDH was prepared without magnetic or organic species for comparison. Al/Zn LDH was prepared through mixing aqueous solutions (0.069 mol/L) of aluminum nitrate

with zinc nitrate in the presence of 0.5 mol/L of urea. The molar ratio of aluminum to zinc was 1:3. By keeping the temperature of the mixture at 80 °C, the nanolayers of LDH were precipitated during the hydrolysis of urea because the nature of the reaction medium was gradually changed from acidic to alkaline. White precipitate was obtained after 12 h of reaction. It was filtrated and washed with distilled water. After drying at room temperature, the product was collected and coded by ZA.

The inorganic-magnetic-organic nanohybrid was synthesized by adding 100 mL of the aqueous solution of 5% n-capric acid sodium salt during building the Al/Zn nanolayered structure. Moreover, 0.5 g of the prepared nanoparticles of cobalt iron oxides nanocomposite was mixed with the aqueous solution (0.069 mol/L) of aluminum nitrate with zinc nitrate in the presence of 0.5 M of urea. By keeping the temperature of the mixture at 80 °C, the product was obtained after 12 h of reaction. After filtration and washing, the product was dried under vacuum at room temperature. The sample was coded by NHZ-1.

Another inorganic-magnetic-organic nanohybrid was prepared by the same procedure, changing the organic compound n-capric acid to be stearic acid. The nanolayers of the Al/Zn LDH were precipitated in the presence of 0.5 g of the prepared nanoparticles of cobalt iron oxides nanocomposite. The product was collected and coded by NHZ-2.

2.3. Preparation of Nanohybrids Based on Oxides

The nanolayered structure of Al/Zn LDH was thermally treated at 500 °C for 5 h in the presence of air to produce a nanocomposite of zinc and aluminum oxides through an Integrated-Type Intelligent Furnace (SX2-2.5-10Z, Lead-Teck, Shanghai, China). It was represented by ZA-500. Through calcination at 500 °C in the presence of air for 5 h, the nanohybrid NHZ-1 was converted to a stable nanohybrid composed of magnetic and non-magnetic oxides. It was represented by NHZ-1-500. The organic-inorganic-magnetic nanohybrid NHZ-2 was transformed to a new structure of nanohybrid through the thermal treatment at 500 °C in presence of air for 5 h. It was represented by NHZ-2-500.

2.4. Physical Characterization

Nanolayered structures and crystalline structures of the prepared samples were identified by a Bruker-AXS system (Bruker Company, Karlsruhe, Germany) with Cu-K α radiation for X-ray diffraction analysis (XRD). A scanning electron microscopy was used for imaging the sample in a large area JEOL JSM-6330F (Tokyo, Japan). An electron probe micro analyzer JED 2300 (JEOL Company, Tokyo, Japan) was used for detecting the elements and its chemical composition in the prepared samples through energy dispersive X-ray spectroscopy (EDX). For studying the thermal behavior of the prepared samples, the thermogravimetric analyzer TA series Q500 and differential scanning calorimetry (DSC) TA series Q600 (TA company, New Castle, PA, USA) were used under the flow of nitrogen. For imaging the nano size and morphology of the prepared materials, transmission electron microscopy (TEM) JEM 2100F (JEOL Company, Tokyo, Japan) was used with different magnifications. The optical properties were measured for the prepared samples through the diffuse reflectance technique. A UV/VIS/NIR Shimadzu 3600 spectrophotometer (Shimadzu, Columbia, MD, USA) was used for measuring the absorbance of liquid and solid samples.

2.5. Photocatalytic Activity

Photocatalytic degradation of aqueous solutions of industrial dyes was used for measuring the photocatalytic activity of the prepared materials for purification of water. Photocatalytic reactions were carried out inside the quartz immersion well reactor RQ400, which was supplied by a photochemical reactors limited company in Camberley Surrey, UK. The photocatalytic reactions were accomplished inside a 400 mL standard reaction flask Model 3308, which is fabricated of quartz glass. A 400-watt power supply 3140/PX0783 was used with 400 W medium pressure mercury lamp 3040/PX0686. In the current study, an aqueous solution of Naphthol green B, which was used as a pollutant, was prepared

with a low concentration 4×10^{-4} mol/L. According to the law of Beer–Lambert, when the initial concentration of dye is low, the intensity of the measured spectrum of the dye can be used to express the dye concentration. Thus, the changes in the concentrations of Naphthol green B were monitored by measuring the absorbance at 714 nm, which considered the characteristic band of Naphthol green B. By using a photocatalytic reactor, 300 mL of the green solution was mixed with 0.1 g of the prepared materials and irradiated by UV light at room temperature. To maintain the temperature of the photocatalytic reaction, the glass reactor was equipped with a cooling system. Before irradiation of UV light and after stirring the mixture for 10 min in the dark, the concentration of the green mixture was measured for detecting the adsorption of the dye on the catalyst [1]. At different intervals of irradiation time, a fixed amount of the solution was extracted and measured by UV-Vis spectrophotometer to determine the concentration of the remaining dye in the solution.

3. Results

3.1. Characterization of the Prepared Filler

Very fine nanoparticles of cobalt iron oxides nanocomposite were prepared and characterized to be suitable for using as a filler and inserting among the nanolayers of the nanolayered structures. In this trend, X-ray diffraction was used to confirm the structure of the prepared cobalt iron oxides nanocomposite. Figure 2a shows an X-ray diffraction pattern of the prepared cobalt iron oxides nanocomposite.

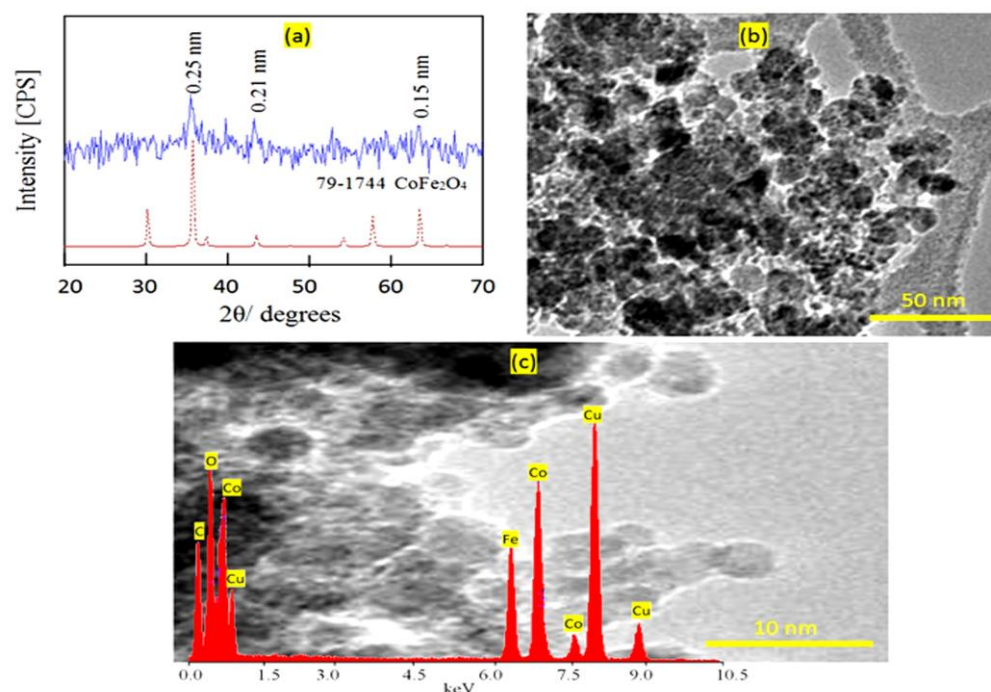


Figure 2. The prepared cobalt iron oxides nanocomposite (a) X-ray diffraction pattern, (b) TEM image at 50 nm, and (c) TEM image at 10 nm (inset: EDX spectrum).

The X-ray diffraction pattern showed weak peaks at $2\theta = 35.56^\circ$, 41.6° , and 62.9° agreeing with d-spacings at 0.25 nm, 0.21 nm, and 0.15 nm, respectively. By comparing with the standard diffraction pattern of JCPDS 79-1744, Figure 1 reveals that the prepared cobalt iron oxides have CoFe_2O_4 structure. Transmission electron microscopy was used for measuring the nano size of the particles of the prepared cobalt iron oxides. Figure 2b shows strong aggregates of nanoparticles because of the magnetic behavior of the cobalt iron oxides. By magnification, very fine nanoparticles were observed in Figure 2c. Figure 2c show that the size of the particles of the prepared cobalt iron oxides is less than 5 nm. Energy dispersive X-ray spectrometry (EDX) analysis confirmed the presence of magnetic elements by observing two sharp peaks for cobalt and iron as shown in Figure 2c (inset).

3.2. Design of Inorganic-Magnetic-Organic Nanohybrids

Inorganic-magnetic-organic nanohybrids appear to be very creative because they can produce unlimited sets of known or unknown properties. In this way, nanohybrids were designed by combining one-dimensional nanoparticles of magnetic nanocomposite and two-dimensional nanolayered structures in addition to long chains of organic acid. This combination was achieved in an order arrangement by building Al/Zn nanolayered structures which have cationic nanolayers. In the presence of n-capric acid ($\text{CH}_3(\text{CH}_2)_8\text{COO}^-$), the long chains of the aliphatic acid were intercalated among the nanolayers for neutralizing their positive charges. At the same time, the long chains of organic compound were working as pillars for building the nanolayered structures. In addition, these pillars expanded and widened the interlayered spacing among the nanolayers to produce enough space for existing magnetic nanoparticles cobalt iron oxides. To indicate the positive role of organic species for designing this nanohybrid, the pure Al/Zn nanolayered structure was prepared for comparison. Moreover, the Al/Zn nanolayered structure was modified by the nanoparticles of cobalt iron oxides nanocomposites with longer chains of organic fatty acid to study the effect of the organic species. X-ray diffraction patterns of the prepared nanolayered structures and nanohybrids are displayed in Figure 3.

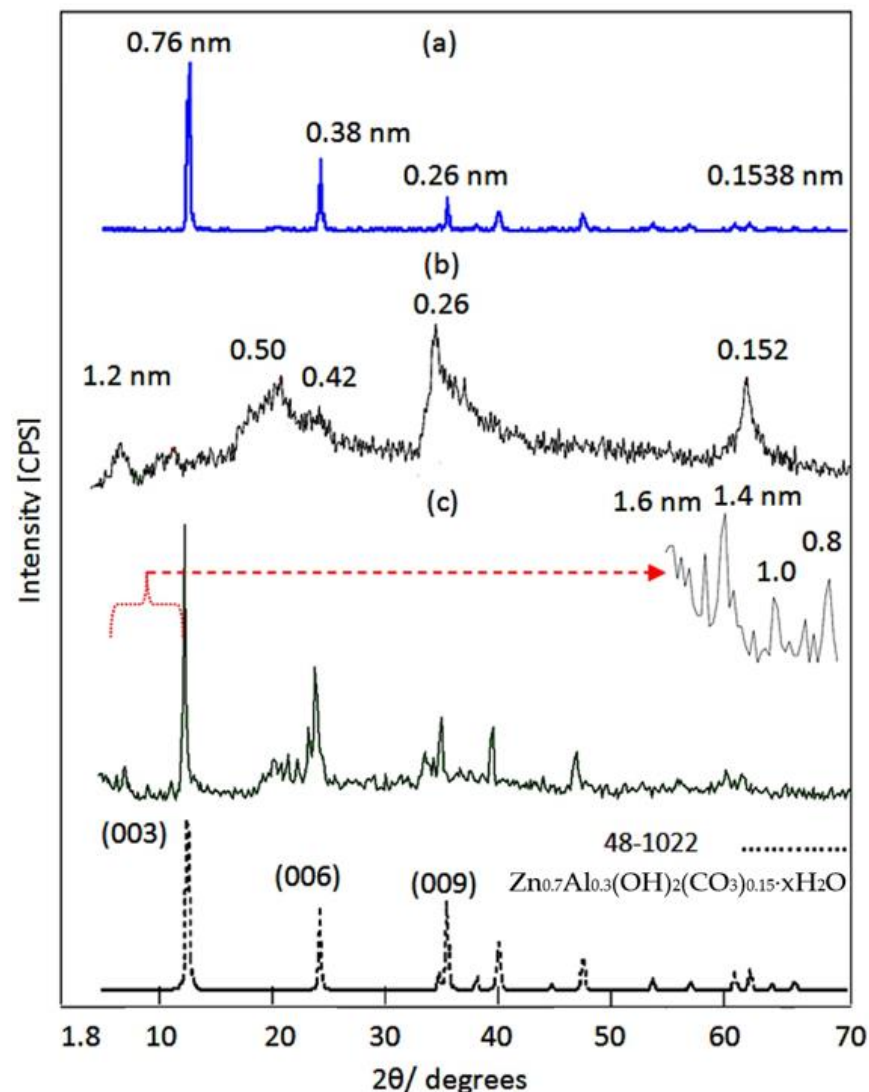


Figure 3. X-ray diffraction patterns of: (a) the pure Al/Zn nanolayered structure, (b) the nanohybrid ZNH-1 and, (c) the nanohybrid ZNH-2.

Figure 3a shows the x-ray diffraction pattern of the pure Al/Zn nanolayered structure. Sharp and symmetric peaks were observed at 2 theta 11.62° , 23.36° , and 34.54° aligning with d-spacing of 0.76 nm, 0.38 nm, and 0.26 nm. These peaks are due to the reflections of the main planes [003], [006], and [009]. The clear arrangement between these reflections ($0.76\text{ nm} = 2 \times 0.38\text{ nm} = 3 \times 0.26\text{ nm}$) confirmed formation of the nanolayered structures of the natural hydrotalcite (JCPDS file No. 37–629) and zinc aluminum carbonate hydroxide hydrate (JCPDS file No. 38–486). The other reflections of the planes [012], [015], [110], and [113] of the nanolayered structures of the natural hydrotalcite were observed at 2 theta 39.16° , 46.56° , 60.05° , and 61.44° and matching with d-spacing 0.23 nm, 0.19 nm, 0.17 nm, and 153 and 0.150 nm. The crystal parameters (a, c) were calculated depending on the d-spacing of the planes [003] and [110], respectively. The first parameter was $2 \times d_{[110]} = 0.306\text{ nm}$. This means that the average distance between the Zn cation and Al cation was 0.306 nm agreeing with the previous published data of zinc aluminum carbonate hydroxide hydrate (JCPDS file No. 38–486). The second parameter was assessed by $3 \times d_{[003]} = 2.28\text{ nm}$. It was similar to that reported for the natural hydrotalcite.

By intercalating the long chains of n-capric acid ($\text{CH}_3(\text{CH}_2)_8\text{COO}^-$) with the Al/Zn nanolayered structures in the presence of the nanoparticles of cobalt iron oxides, inorganic-magnetic-organic nanohybrid NHZ-1 was formed through host-guest interaction. The X-ray diffraction pattern of NHZ-1, which is displayed in Figure 3b, showed new peaks at low 2 theta in addition to the disappearance of the original peaks of the nanolayered structure of LDH. The peaks of the nanoparticles of magnetic nanocomposite are unclear. A weak peak is observed at 1.20 nm indicating that the interlayered spacing of the nanolayered structure expanded and widened from 0.755 nm to 1.20 nm. This spacing may be allowed for the nanoparticles of cobalt iron oxides to intercalate among the nanolayers of the nanolayered structure because the peaks of cobalt iron oxides are not clear in Figure 3b. The crystal parameter (a), which depends on the reflection of the plane [110], has a little shift. At the same time, a large change is observed for parameter (c) from 2.280 nm to 3.60 nm. This means that the nanohybrid NHZ-1 consists of nanolayered structures having organic species and magnetic nanoparticles.

With intercalating longer chains of organic compounds, stearic acid ($\text{CH}_3(\text{CH}_2)_{16}\text{COO}^-$), and the nanoparticles of cobalt iron oxides nanocomposite inside the pure Al/Zn nanolayered structures, NHZ-2 was formed to build another inorganic-magnetic-organic nanohybrid. Figure 3c shows the main peaks of the Al/Zn LDH in addition to new peaks after building the nanohybrid NHZ-2. The new peaks of the nanohybrid NHZ-2 were observed at 1.6 nm and 1.4 nm as seen in Figure 3c (inset).

This indicated that the interlayered spacing of the nanolayered structure expanded and widened from 0.755 nm to become higher. This expansion allows for the nanoparticles of cobalt iron oxides to intercalate among the nanolayers of the nanolayered structure because the peaks of cobalt iron oxides are not clear in Figure 3c. This means that the nanohybrid NHZ-2 consists of nanolayered structures having organic species and magnetic nanoparticles.

This finding was confirmed by transmission electron microscopy (TEM) and energy dispersive X-ray spectrometry (EDX) analysis. TEM images of the nanohybrid NHZ-1 are displayed in Figure 4.

Figure 4a shows that the nanohybrid ZNH-2 has nano-platelets with sizes less than 50 nm. Moreover, very fine nanoparticles, marked by arrow, are observed in Figure 4c,d representing the magnetic nanoparticles cobalt iron oxides. By magnification, Figure 4c suggests the presence of the magnetic nanoparticles among the nanolayers of nanohybrid. In addition, Figure 4d shows one particle that started to intercalate with the nanolayered structure. This suggestion was confirmed by EDX analysis. Figure 4e shows sharp peaks for the non-magnetic elements zinc and aluminum. In addition, the magnetic elements cobalt and iron were observed by weak peaks.

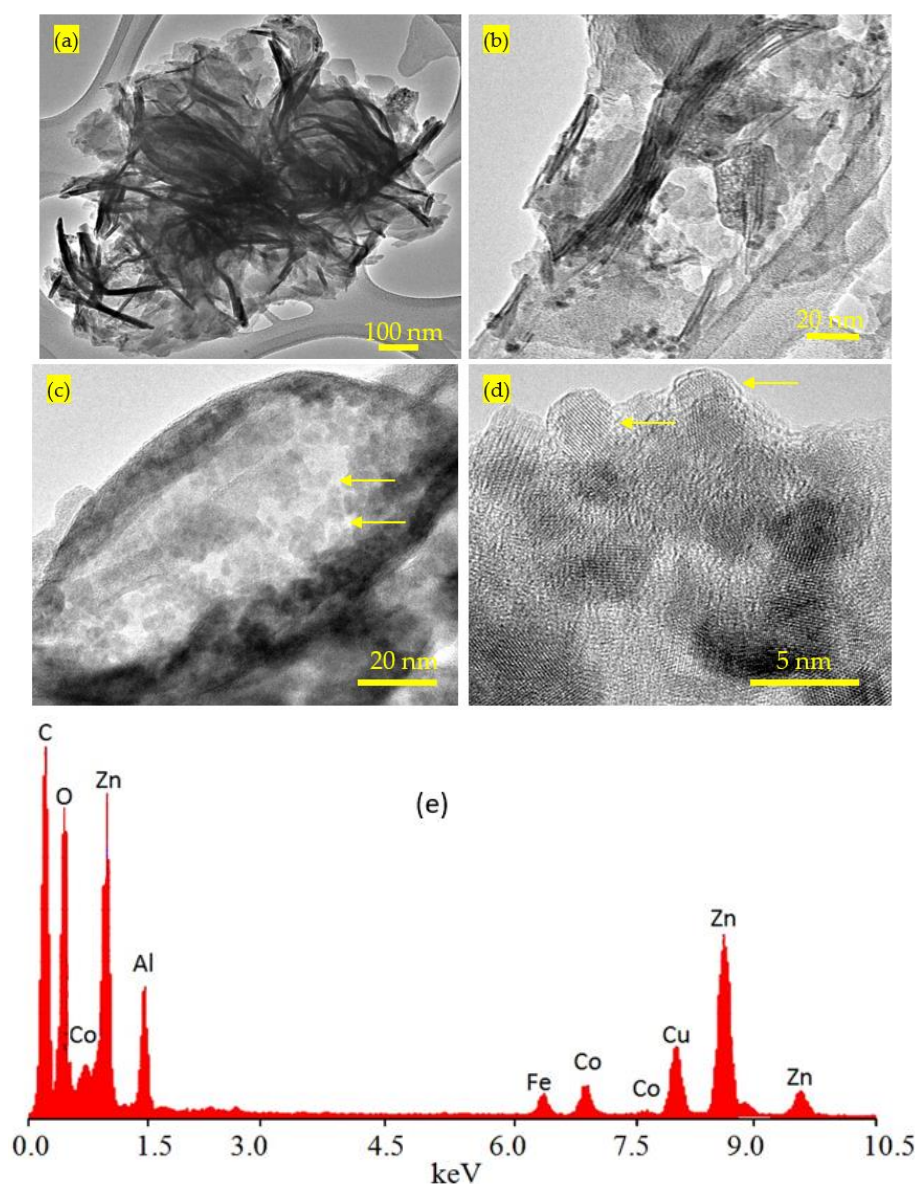


Figure 4. TEM images of the nanohybrid NHZ-1: (a) at 100 nm, (b,c) at 20 nm, (d) at 5 nm (yellow arrows for the intercalated nanoparticles) and, (e) EDX spectrum.

The Fourier Transform infrared (FT-IR) spectroscopy was applied to compare the function groups of the nanohybrids NHZ-1 and NHZ-2 as shown in Figure 5. For the nanohybrid NHZ-1, the absorption band was observed at 3434 cm^{-1} indicating the stretching mode of hydroxyl groups as seen in Figure 5a. The presence of long chains of hydrocarbon of n-capric acid was clear in the IR spectrum because the stretch absorption of carbon-hydrogen was observed by sharp peaks at 2924 cm^{-1} and 2953 cm^{-1} . Furthermore, the bending mode of the carbon-hydrogen was clear through observing the band at 1468 cm^{-1} . The symmetric stretching vibration of carboxylate, which belonged to the aliphatic acid, was observed at 1554 cm^{-1} . Furthermore, the absorption at 1411 cm^{-1} is assigned to the asymmetric stretching vibration of carboxylate. The bands observed below 1000 cm^{-1} can be ascribed to Zn-O and Al-O. For the nanohybrid NHZ-2, Figure 5b confirms formation of inorganic-magnetic-organic nanohybrid through observing the main bands of stearic acid. The presence of long chains of hydrocarbon was confirmed by observing sharp peaks at 2922 cm^{-1} and 2849 cm^{-1} indicating the stretch absorption of carbon-hydrogen. Moreover, the bending mode of the carbon-hydrogen was clear through observing band at 1466 cm^{-1} . The symmetric stretching vibration of carboxylate, which belonged to the aliphatic acid,

was observed at 1589 cm^{-1} . Furthermore, the absorption at 1397 cm^{-1} was assigned to the asymmetric stretching vibration of carboxylate. In addition, the absorption band of the hydroxyl groups of the nanolayered structure was observed at 3467 cm^{-1} . In the same trend, the presence of different kinds of hydroxyl groups were confirmed by observing another band for hydroxyl groups at 3694 cm^{-1} . This indicated that the presence of the nanoparticles of cobalt iron oxides among the nanolayers affects the vibrational mode of hydroxyl groups which means that the confinement of the nanoparticles of CoFe_2O_4 among the nanolayers affects the hydroxyl groups which are near these nanoparticles.

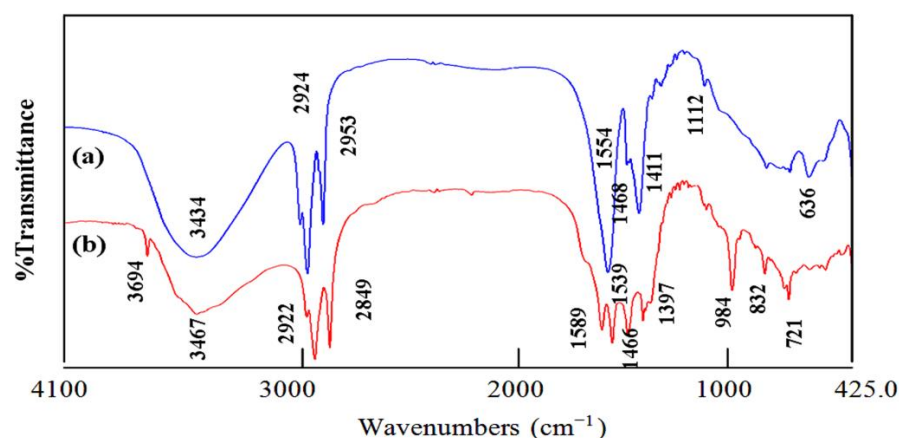


Figure 5. FT-IR spectra of: (a) the nanohybrid NHZ-1 and (b) the nanohybrid NHZ-2.

The thermal gravimetric analysis and differential scanning calorimetric (TGA-DSC curves) showed that the degradation occurs through a continuous process with various mass rate losses depending upon the nature of the interlayer species. The DSC curve of the nanohybrid NHZ-1 showed two series of peaks as shown in Figure 6a. The first series is endothermic peaks at 92°C and 171°C which are ascribed to the removal of the surface and interlayered water. The second series is exothermic peaks at 250°C , 419°C , and 552°C representing the oxidation reactions of the chains of hydrocarbon of n-capric acid. From the TG curve (Figure 6c), the weight loss was 18%, which happened up to 222°C , and represents the internal content of water inside the nanohybrid NHZ-1. In the same way, the weight loss of 36%, which occurred up to 460°C was due to the internal content of organic species inside the nanohybrid NHZ-1. The DSC curve of the nanohybrid NHA-2 was similar to that of the nanohybrid NHZ-2 as seen in Figure 6b. Figure 6b shows the endothermic and exothermic peaks indicating the removal of water and oxidation reactions of the long chains of hydrocarbon of stearic acid. Similar behavior was observed for the TG curve of NHZ-2 as shown in Figure 6d. The thermal analyses results confirmed formation of the nanohybrids NHZ-1 and NHZ-2.

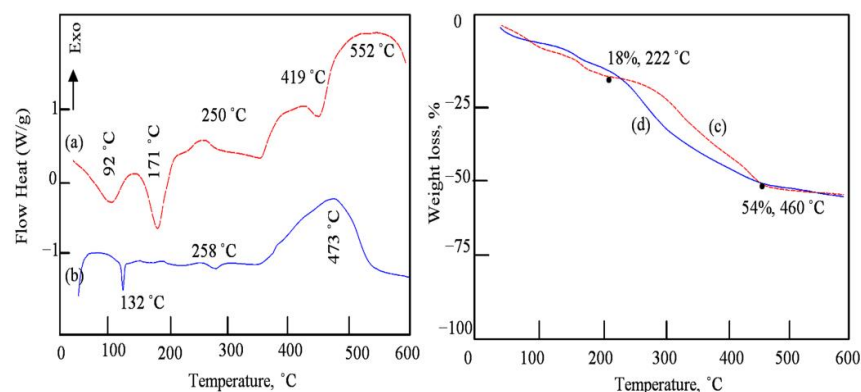


Figure 6. Thermal analyses of (a) DSC curve of NHZ-1, (b) DSC curve of NHZ-2, (c) TG curve of NHZ-1, and (d) TG curve of NHZ-2.

3.3. Design of Nanohybrids Based on Oxides

The main reason for designing nanohybrids with organic and inorganic species is to produce stable and effective zinc oxides nanohybrids and nanocomposites with distinguished properties. Therefore, the prepared nanohybrids were thermally treated at 500 °C to remove unstable species and create new active sites.

X-ray diffraction was used to identify the produced structures from the calcination of the nanohybrids. Figure 7 showed X-ray diffraction patterns of ZA-500, NHZ-1-500, and NHZ-2-500. The XRD pattern of ZA-500 exhibited new weak peaks at $2\theta = 32.01^\circ$, 34.32° , 36.49° , 47.71° , 7.05° , and 62.81° in addition to the disappearance of the original peaks of the nanolayered structures as shown in Figure 7a. By comparing the diffraction lines of the zinc oxide crystal (JCPDS No. 36-1451) and the standard entire diffraction pattern of zincite phase (JCPDS No. 75-576) [2,7], ZA-500 has a similar structure to zinc oxide. In the case of the nanohybrid NHZ-1-500, Figure 7b shows clear and sharp peaks at 0.28 nm, 0.26 nm, and 0.24 nm indicating a crystalline structure. Moreover, weak peaks were observed at 0.19 nm, 0.16 nm, 0.15 nm, and 0.14 nm. These diffraction lines agree with the peaks of the zinc oxide crystal (JCPDS No. 36-1451) and the standard entire diffraction pattern of zincite phase (JCPDS No. 75-576). In addition, a weak peak was observed at 0.30 nm and marked with (*) in Figure 7b. At the same time, Figure 7b reveals that the characteristic peak of cobalt iron oxides at 0.25 nm overlapped with the peak of zinc oxide at 0.24 nm. For the nanohybrid NHZ-2-500, Figure 7c shows that the characteristic peaks of zinc oxide were observed at 0.28 nm, 0.26 nm, and 0.24 nm agreeing with the crystalline structure of the sample NHZ-1-500. This similarity was confirmed by observing weak peaks at 0.19 nm, 0.16 nm, 0.15 nm, and 0.14 nm. These diffraction lines agree with the peaks of the zinc oxide crystal (JCPDS No. 36-1451) and the standard entire diffraction pattern of zincite phase (JCPDS No. 75-576). At the same time, Figure 7c reveals that the characteristic peak of cobalt iron oxides at 0.25 nm were not clear in the sample NH-2-500. These XRD results can conclude that both NHZ-1-500 and NHZ-2-500 have zincite phase doping with aluminum and cobalt iron oxides.

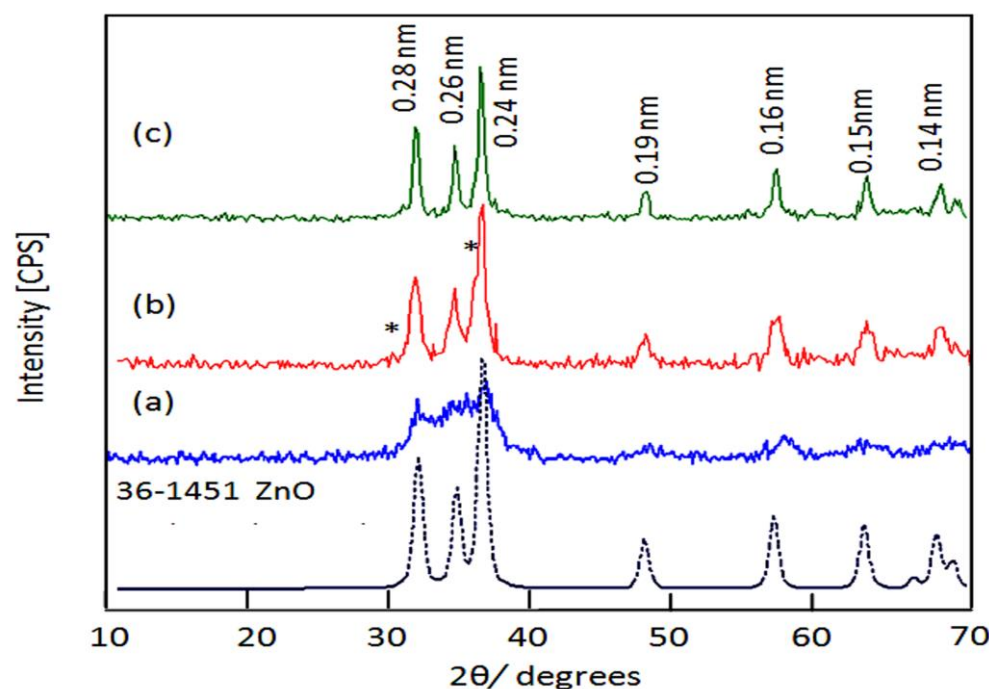


Figure 7. X-ray diffraction patterns of: (a) ZA-500, (b) NHZ-1-500, and (c) NHZ-2-500 (* is due to cobalt iron oxides).

TEM images of ZNH-1-500 confirmed this finding as shown in Figure 8. Clear nanoparticles were observed for NHZ-1-500 as seen in Figure 8a. This indicated that the width of

NHZ-1-500 is 20 nm. Figure 8b shows combination between the zinc oxide particles with the particles of cobalt iron oxides. Energy dispersive X-ray spectrometry (EDX) analysis of NHZ-1-500 confirmed the presence of magnetic elements by observing two weak peaks for cobalt and iron as seen in Figure 8c. Furthermore, the inorganic elements (zinc, aluminum, and oxygen) were also observed through sharp peaks as seen in Figure 8c.

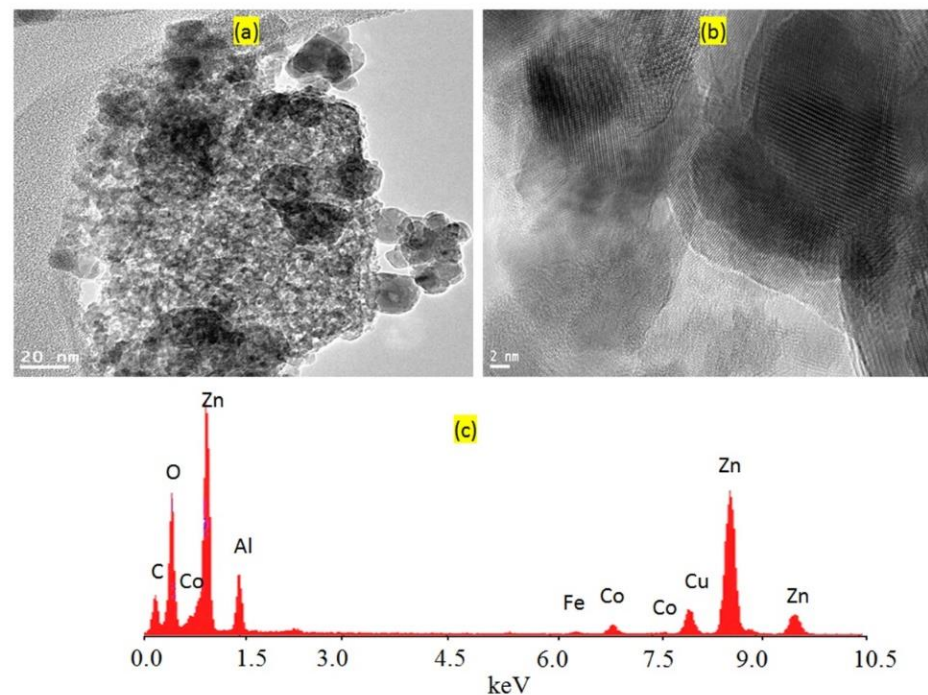


Figure 8. TEM images and EDX of NHZ-1-500: (a) 20 nm, (b) 2 nm, and (c) EDX spectrum.

To determine the chemical composition of NHZ-1-500, scanning electron microscopy (SEM) and energy dispersive X-ray spectrometry (EDX) were used to detect the quality and quantity of the different elements in the sample. SEM images showed clear nanoparticles for NHZ-1-500 as shown in Figure 9a. The EDX spectrum, which is attached to SEM, confirmed the presence of magnetic elements Co and Fe. Moreover, Figure 9b shows that the atomic percentages of cobalt and iron in the sample NHZ-1-500 are 1.24% and 0.96%, respectively. In addition, the atomic percentage of aluminum rose to 18.64%. At the same time, Figure 9b reveals that the highest percentage was due to zinc. This means that NHZ-1-500 is composed of zinc oxide structure doping with Al, Co, and Fe confirming the XRD results.

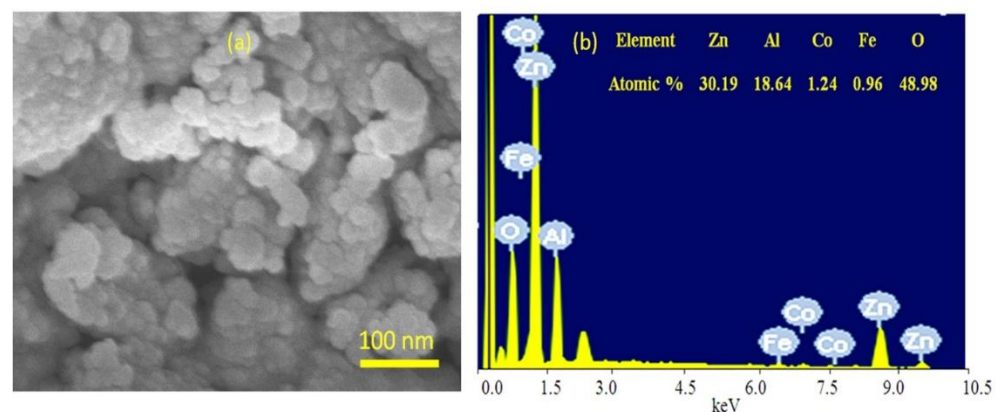


Figure 9. Images and spectrum of NHZ-1-500: (a) SEM and (b) EDX.

3.4. Optical Properties

Zinc oxide is familiar for the researchers in the field of optical application as one of the most famous photo-active materials. However, its optical applications are concentrated in the UV region; therefore, many studies have been published for developing the structure and the morphology of zinc oxide to advance its optical behavior through increasing the range of its absorbance and decreasing its band gap energy.

In this way, the optical absorbance and the band gap energy of the prepared nanohybrids were studied and compared using the UV-Vis absorption technique which is considered a powerful tool for providing important details about optical properties.

Figure 10 shows the UV-Vis absorbance of ZA-500, NHZ-1-500, and NHZ-2-500. Figure 10a indicates that ZA-500 is active in the UV region because it has absorption in the range of wavelength 200–350 nm. In the same time, there is no absorption in the visible region above 400 nm as shown in Figure 10a. By modifying the structure of ZA-500 by building a nanohybrid with magnetic nanocomposites and n-capric acid, the optical properties of NHZ-1-500 improved as shown in Figure 10b. The new absorbance band was observed in the visible region at 630 nm. At the same time, the absorbance edge shifted to a higher wavelength at 700 nm. This positive effect was also observed for NHZ-2-500 as shown in Figure 10c. Figure 10c shows clear absorbance for NHZ-2-500 starting from 700 nm to 200 nm with two maxima at 600 nm and 350 nm. This means that the intercalation of magnetic nanoparticles inside the interlayered space of the nanohybrid led to good order dispersion inside the structure of zinc oxide in addition to creating new optical active centers for ZnO after calcination.

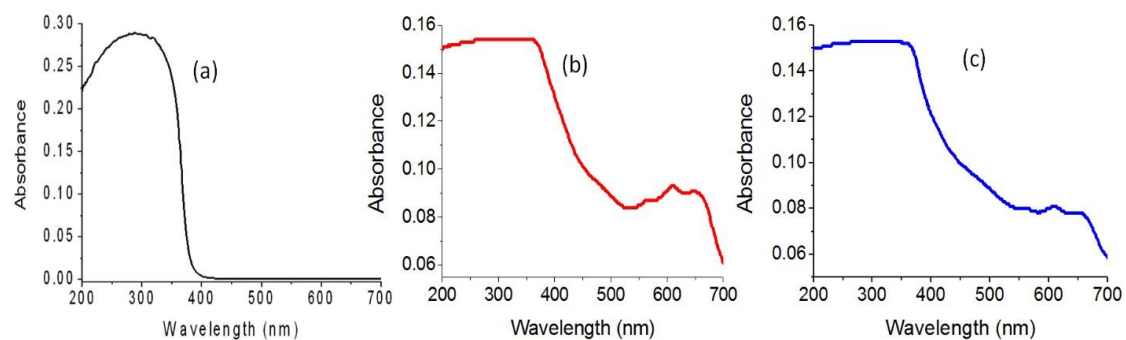


Figure 10. UV-Vis absorbance of (a) ZA-500, (b) NHZ-1-500, and (c) NHZ-2-500.

This finding was confirmed by calculating their band gap energy through a Tauc plot [44–46]. The band gap energy was determined by plotting the relation between $(\alpha h\nu)^2$ and energy ($h\nu$) as shown in Figure 11. The band gap energy E_g of ZA-500 was calculated by extending the straight line to the $(h\nu)$ axis to obtain the optical band gap energy at $(\alpha h\nu)^2$ of 0. This showed 3.10 eV indicating a little shift from the band gap of pure ZnO (3.295 eV) [45] because the doping of aluminum inside the zinc oxide structure caused two competing mechanisms [44,45]; there are band gap widening (BGW) and band gap narrowing (BGN). BGN is a consequence of many body effects on the conduction and the valence bands; narrowing is counteracted by the Burstein–Moss effect, which provides BGW as a result of blocking of lowest states in the conduction band. For a lightly doped semiconductor, the filling of the conduction band leads to BGW. Burstein–Moss provided the band gap broadening in an n-type semiconductor. On the other hand, for higher donor density, band gap narrowing becomes significant [46]. This phenomenon, which affects the optical absorption edge more with increasing donor density, is due to many body effects such as exchange energy due to electron–electron and electron–impurity interactions. These effects lead to a narrowing of the band gap (red shift). In this case, the total measured optical band gap, E_g , is the net result of blue shift and red shift. Wolf [45] showed that the band gap red shift is predominant in heavily doped n-type semiconductors similar to our previous work [44] and the current study.

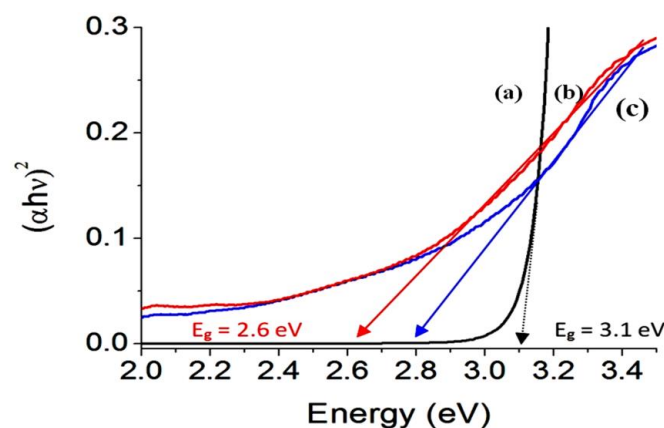


Figure 11. Band gap of (a) ZA-500, (b) NHZ-1-500, and (c) NHZ-2-500.

In the case of NHZ-1-500, a large change was observed for the band gap energy, 2.60 eV, as shown in Figure 11b. This strong effect of the nanohybrid structure was also observed for NHZ-2-500 as shown in Figure 11c. Figure 11c shows that the band gap energy of NHZ-2-500 was 2.79 eV. Compared with the pure zinc oxide, the narrowing of band gap energy was clear because the reduction was from 3.30 eV [45] to 2.60 and 2.79 eV for both nanohybrids indicating that the inorganic-magnetic-organic nanohybrids have a strong positive effect on the optical properties of zinc oxide.

3.5. Fast Removal of Green Dyes

It is known that the improvement of the optical properties of the products of zinc oxides leads to positive effects for their photo activities. In order to indicate these positive effects, the prepared products were used as photocatalysts to be appropriate means for increasing the photocatalytic activity of zinc oxide to decompose and remove pollutants by light in a short time. In this way, the green dye of Naphthol green B was used as an example for colored pollutants. The photo activities of zinc oxides (doped or non-doped), and their products based on the nanohybrids structure were studied through photocatalytic degradation of Naphthol green B. By irradiating the aqueous solution of Naphthol green B with the UV light in the presence of the photocatalyst and measuring the absorbance of the liquid portion after the irradiation of UV for a certain number of minutes, the reduction in the absorption of the green dye at wavelength 714 nm indicated the degradation of the main structure of the pollutant, while the degradation of the naphthyl rings in the dye could be followed from the absorption peaks at 322 nm, 280 nm, and 230 nm as shown in Figure 12a,b.

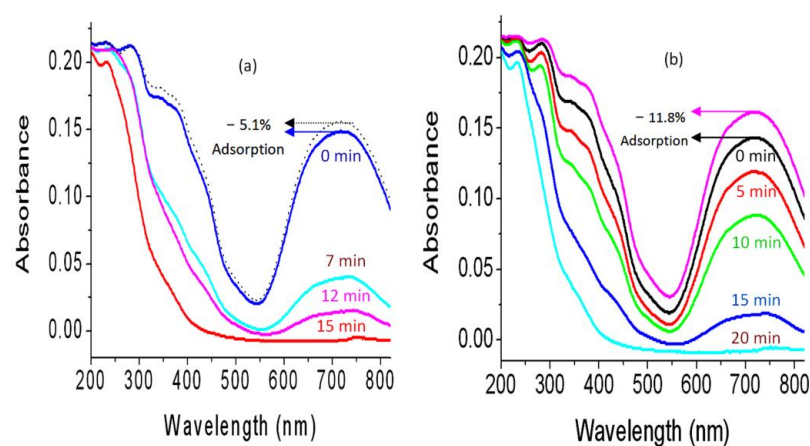


Figure 12. Photocatalytic degradation of Naphthol green B in presence of: (a) NHZ-1-500 and (b) ZNH-2-500.

The blank experiment was performed without photocatalyst for 20 min of UV-irradiation. The concentration did not change, indicating high stability of the Naphthol green B toward the light irradiation as shown in the first curve of Figure 12a,b. The photocatalytic degradation of the green dye was investigated as a function of the UV light irradiation time in the presence of the photocatalyst as seen in Figure 12. When the aqueous solution of Naphthol green B was mixed with the photocatalyst for 10 min in the dark, an appropriate change was observed indicating that these photocatalysts have adsorption power. By calculating the removal percentage of the green dyes through the adsorption process, Figure 12a shows that the sample NHZ-1-500 removed 5.1%. In the case of the sample ZNH-2-500, 11.8% was removed by the adsorption process. Therefore, in order to determine the removal percentage of the green dyes through photocatalytic degradation, the second curve in Figure 12a,b was used as 0 min irradiation.

Figure 12a shows the photocatalytic degradation of Naphthol green B under UV light in the presence of NHZ-1-500. By increasing the irradiation time, the photocatalytic degradation of Naphthol green B increased. After 15 min of UV irradiation time, a complete removal of the green color was observed indicating high activity for NHZ-1-500. In the case of using NHZ-2-500, the activity became a little lower as shown in Figure 12b. A complete photocatalytic degradation of the Naphthol green B was achieved after 20 min of UV irradiation time. This means that NHZ-1-500 was very active because it completely destroyed the green dye at shorter time.

The high performance of the zinc oxide nanohybrids NHZ-1-500 and NHZ-2-500 was clear after comparison with the ZA-500 as shown in Figure 13. Where the removal of the green dye gradually happened and was completed after 90 min of UV irradiation time in the presence of ZA-500 as shown in Figure 13a. While Figure 13b,c shows that the removal percentages of the dyes decreased sharply in the case of using NHZ-2-500 and NHZ-1-500, respectively. In order to indicate the effect of organic species, the kinetics of photocatalytic decolorization and degradation of Naphthol green B were studied for both NHZ-1-500 and NHZ-2-500 by the following equation:

$$\ln([C_0]/[C]) = kt \quad (1)$$

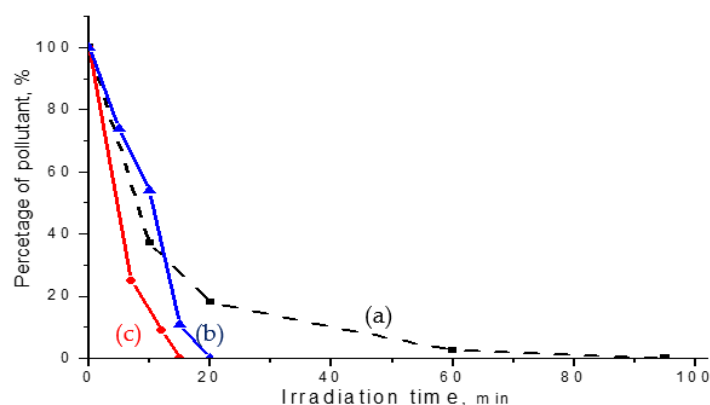


Figure 13. Percentage of the Naphthol green B after different irradiation times in presence of: (a) ZA-500, (b) NHZ-2-500, and (c) NHZ-1-500.

The concentration of Naphthol green B at different times is coded as $[C]$. The initial concentration of Naphthol green B, which was expressed by the absorbance at time equal zero, is coded as $[C_0]$. The rate reaction constant is k . By plotting the irradiation time in minutes against $\ln([C_0]/[C])$, the diagrams can be employed for kinetically determining the type of reactions.

According to Figure 14, the diagrams indicated that the photocatalytic degradation and decolorization of Naphthol green B are pseudo-first-order reactions in the case of using both NHZ-1-500 and NHZ-2-500. Figure 14b shows that the rate reaction constant

of the photocatalytic degradation of Naphthol green B in the presence of ZNH-2-500 is 0.145 min^{-1} . By using NHZ-1-500, the reaction became faster because the rate reaction constant increased to 0.220 min^{-1} as shown in Figure 14a. The kinetics study concluded that the rate of photocatalytic degradation of Naphthol green B in the presence of NHZ-1-500 increased to be higher than that of ZNH-2-500. This means that the activity of the sample NHZ-1-500, which was prepared from a pure nanohybrid, is higher than the activity of the sample NHZ-2-500, which was produced from a mixed phase of nanohybrid and nanolayered structures.

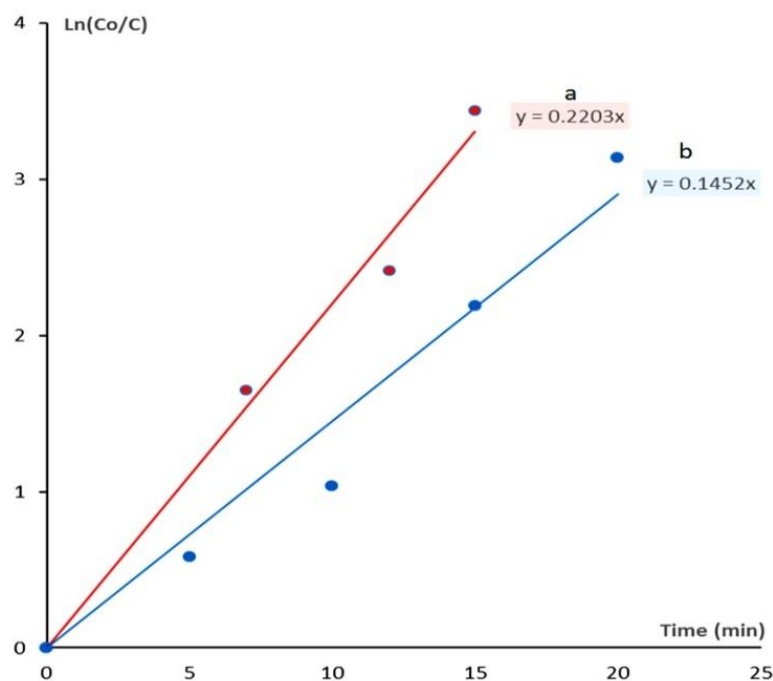


Figure 14. Kinetics study of the photocatalytic degradation of Naphthol green B in presence of: (a) NHZ-1-500 and (b) NHZ-2-500.

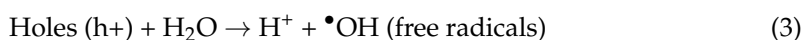
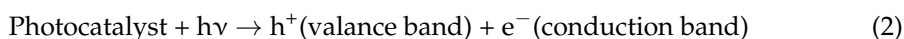
The recyclability of the prepared photocatalysts was tested through repeating the process of photocatalytic degradation of NHZ-1-500 two times for the fresh sample of the green dye. Similar results were observed after 15 min of light irradiation indicating high recyclability of the produced photocatalysts. This conclusion showed the important role of a nanohybrid structure for producing stable and effective photocatalysts.

4. Discussion

The fast photocatalytic degradation of the green dyes showed the excellent activity of the prepared zinc oxide nanohybrid NHZ-1-500 which was produced from inorganic-magnetic-organic nanohybrids. The high performance of NHZ-1-500 can be explained through the novel strategy for building the nanohybrid structure of NHZ-1-500. The intercalation of the fine nanoparticles of CoFe_2O_4 nanocomposite among the nanolayers of Al/Zn provided a good chance for incorporation of this nanocomposite with zinc oxide structures during the crystallization process. Therefore, NHZ-1-500 has good crystalline structure for zinc oxide and there are no peaks for aluminum or cobalt iron oxides. This good incorporation of CoFe_2O_4 nanocomposite with the crystals of zinc oxide is partially failed for the sample NHZ-2-500 because XRD results showed two mixed phases; nanolayered structure and nanohybrid. This means that the nanoparticles of CoFe_2O_4 nanocomposite could intercalate among the nanolayers of Al/Zn for part of the nanohybrid and support on the external surface of the plates of the nanolayered structure of Al/Zn. The good incorporation of CoFe_2O_4 nanocomposite with the crystals of zinc oxide which were doped with aluminum created new optical active centers inside the zinc oxide nanohybrid NHZ-1-500

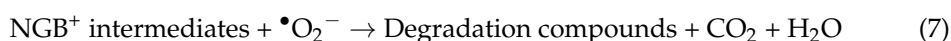
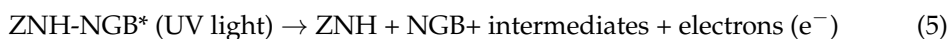
and caused reduction for its band gap energy to be very effective in light because of the low band gap energy of CoFe_2O_4 (1.32 eV) [43]. At the same time, some sites of Zn in zinc oxide are occupied by CoFe_2O_4 atoms producing new optical active centers called shallow traps between the valance band and conduction band leading to decreasing for the band gap energy [1,46].

This low band gap energy and the small size of the nanoparticles of the zinc oxide nanohybrid NHZ-1-500 have a strong effect on the mechanism of the photocatalytic degradation process of the green dyes. The mechanism of the photocatalytic degradation process is controlled by two critical reactions.



The first one depends on the amount of energy which absorbed by the photocatalyst as seen in the Reaction (2). The second reaction is the movement and separation of light-induced electrons and holes as shown in the Reactions (3) and (4). The photo-generated holes, which produced in the conduction band, react with the water molecules to produce highly oxidizing agents, free radicals of hydroxyl groups ($\bullet\text{OH}$). At the same time, the photo-generated electrons attack the oxygen molecules which are adsorbed on the surface of the photocatalyst or dissolved in water to produce strong oxidizing agents superoxide radical anion ($\bullet\text{O}_2^-$).

In presence of the green dyes, the molecules of NGB adsorbed on the surface of the nanoparticles of the zinc oxide nanohybrid. The NHZ-1-500 accelerated the first reaction to become in the excited state because it has absorbance from the wavelength 700 nm to 200 nm in addition to low band gap energy as shown in Reaction (5).



The band gap of NHZ-1-500 is not very small to accelerate the recombination reactions in addition to the shallow traps which help separate between electrons and holes. Therefore, the degradation reaction continues as shown in Reactions (6) and (7). By this way, the colored pollutants disappeared after 15 min of UV light irradiation.

5. Conclusions

In the present study, a dual aim was achieved for designing a zinc oxide nanohybrid to be useful and effective for purifying water in UV light. This aim focused on a new strategy for building inorganic-magnetic-organic nanohybrids in addition to producing an effective zinc oxide nanohybrid. Two nanohybrids were prepared by expanding the nanolayered structures of Al/Zn by intercalating long chains of hydrocarbons of fatty acids such as n-capric and stearic acid to facilitate the insertion of very fine nanoparticles of cobalt iron oxides among the nanolayers of Al/Zn. The characterization techniques showed that the prepared nanohybrid were useful for producing a zinc oxide nanohybrid by thermal treatment. By measuring the optical properties, a clear reduction in the band gap energy was observed for the prepared zinc oxide nanohybrids comparing with the doped and un-doped zinc oxide. This reduction in the band gap energy from 3.20 eV to 2.60 eV led to high activity for the prepared zinc oxide nanohybrid in UV light.

This high activity was proven by a complete removal of Naphthol green B after 15 min of UV light irradiation in the presence of the prepared zinc oxide nanohybrid. These results were confirmed by the comparison with the Al-doped zinc oxide, which indicated that the pure and doped zinc oxide removed the green dyes after 90 min of light. Furthermore,

the kinetic study showed that the zinc oxide nanohybrid, which was based on a pure nanohybrid that is better than the zinc oxide nanohybrid, was produced from mixed phases between a nanohybrid and nanolayered LDH. Finally, it can be concluded that this strategy for designing a photo-active nanohybrid led to positive tools for facing environment and water-related problems by using a fast technique for purifying water.

Author Contributions: Conceptualization, O.S.; methodology, O.S. and A.O.; software, A.A., M.O. and N.M.S.; validation, O.S. and A.O.; formal analysis, O.S., M.O. and A.O.; investigation, O.S., A.A., N.M.S. and D.O.; resources, O.S.; data curation, O.S., M.O., A.O. and D.O.; writing—original draft preparation, O.S., A.O. and D.O.; writing—review and editing, O.S., A.A. and N.M.S.; visualization, A.O.; supervision, O.S. and A.A.; project administration, O.S.; funding acquisition, O.S. All authors have read and agreed to the published version of the manuscript.

Funding: This research was funded by Al Bilad Bank Scholarly Chair for Food Security in Saudi Arabia, The Deanship of Scientific Research, The Vice Presidency for Graduate Studies and Scientific Research at the Deanship of Scientific Research at King Faisal University (Saudi Arabia), grant number CHAIR31 and the APC was funded by the same grant number CHAIR31.

Data Availability Statement: Data available in a publicly accessible repository.

Acknowledgments: The authors acknowledge Al Bilad Bank Scholarly Chair for Food Security in Saudi Arabia, The Deanship of Scientific Research, The Vice Presidency for Graduate Studies and Scientific Research at King Faisal University for the financial support under the Research Annual Track (Grant No. CHAIR31).

Conflicts of Interest: The authors declare no conflict of interest.

References

1. Saber, O.; Kotb, H.M.; Osama, M.; Khater, H.A. An Effective Photocatalytic Degradation of Industrial Pollutants through Converting Titanium Oxide to Magnetic Nanotubes and Hollow Nanorods by Kirkendall Effect. *Nanomaterials* **2022**, *12*, 440. [\[CrossRef\]](#)
2. Saber, O.; Shaalan, N.M.; Ahmed, F.; Kumar, S.; Alshoaibi, A. One-Step Multi-Doping Process for Producing Effective Zinc Oxide Nanofibers to Remove Industrial Pollutants Using Sunlight. *Crystals* **2021**, *11*, 1268. [\[CrossRef\]](#)
3. Alshoaibi, A.; Saber, O.; Ahmed, F. Enhancement of Optical Activity and Properties of Barium Titanium Oxides to Be Active in Sunlight through Using Hollandite Phase Instead of Perovskite Phase. *Crystals* **2021**, *11*, 550. [\[CrossRef\]](#)
4. Saber, O.; Alshoaibi, A.; Al-Yaari, M.; Osama, M. Conversion of Non-Optical Material to Photo-Active Nanocomposites through Non-Conventional Techniques for Water Purification by Solar Energy. *Molecules* **2020**, *25*, 4484. [\[CrossRef\]](#) [\[PubMed\]](#)
5. Saber, O.; Kotb, H.M. Designing Dual-Function Nanostructures for Water Purification in Sunlight. *Appl. Sci.* **2020**, *10*, 1786. [\[CrossRef\]](#)
6. Saber, O.; Aljaafari, A.; Osama, M.; Alabdulgader, H. Accelerating the Photocatalytic Degradation of Green Dye Pollutants by Using a New Coating Technique for Carbon Nanotubes with Nanolayered Structures and Nanocomposites. *ChemistryOpen* **2018**, *7*, 833–841. [\[CrossRef\]](#)
7. Saber, O.; Alomair, H.; Abu-Abdeen, M.; Aljaafari, A. Fast degradation of green pollutants through nanonets and nanofibers of the Al-doped zinc oxide. *Acta Metall. Sin.* **2018**, *31*, 533–546. [\[CrossRef\]](#)
8. Fujishima, A.; Honda, K. Electrochemical Photolysis of Water at a Semiconductor Electrode. *Nature* **1972**, *238*, 37–38. [\[CrossRef\]](#) [\[PubMed\]](#)
9. Gui, M.S.; Zhang, W.D. Preparation and modification of hierarchical nanostructured Bi₂WO₆ with high visible light-induced photocatalytic activity. *Nanotechnology* **2011**, *22*, 265601. [\[CrossRef\]](#)
10. Chen, X.B.; Liu, L.; Yu, P.Y.; Mao, S.S. Increasing solar absorption for photocatalysis with black hydrogenated titanium dioxide nanocrystals. *Science* **2011**, *331*, 746–750. [\[CrossRef\]](#) [\[PubMed\]](#)
11. Dindar, B.; Icli, S. Unusual photoreactivity of ZnO under concentrated sun light. *J. Photochem. Photobiol. A Chem.* **2001**, *140*, 263–268. [\[CrossRef\]](#)
12. Yeber, M.C.; Roderiguez, J.; Freer, J.; Baeza, J.; Duran, N.; Mansilla, H.D. Advanced oxidation of a pulp mill bleaching wastewater. *Chemosphere* **1999**, *39*, 1679–1688. [\[CrossRef\]](#)
13. Behnajady, M.A.; Modirshahla, N.; Hamzavi, R. Kinetic study on photocatalytic degradation of C.I. Acid Yellow 23 by ZnO photocatalyst. *J. Hazard. Mater. B* **2006**, *133*, 226–232. [\[CrossRef\]](#) [\[PubMed\]](#)
14. Sun, J.H.; Dong, S.Y.; Wang, Y.K.; Sun, S.P. Preparation and photocatalytic property of a novel dumbbell-shaped ZnO microcrystal photocatalyst. *J. Hazard. Mater.* **2009**, *172*, 1520–1526. [\[CrossRef\]](#)
15. Wang, Q.; Tang, C.; Jiang, C.; Du, D.; Wang, F.; Song, J. Role of Substrate Roughness in ZnO Nanowire Arrays Growth by Hydrothermal Approach. *Acta Metall. Sin. Engl. Lett.* **2016**, *29*, 237–242. [\[CrossRef\]](#)

16. Zhou, W.; Li, X.; Qin, L.; Kang, S. Facile Preparation of Ag₂ZnGeO₄ Flower-like Hierarchical Nanostructure and Its Photocatalytic Activity. *J. Mater. Sci. Technol.* **2017**, *33*, 47–51. [\[CrossRef\]](#)
17. Liu, C.; Xu, H.; Wang, L.; Qin, X. Facile One-Pot Green Synthesis and Antibacterial Activities of GO/Ag Nanocomposites. *Acta Metall. Sin. Engl. Lett.* **2017**, *30*, 36–44. [\[CrossRef\]](#)
18. Bai, X.; Wang, L.; Zong, R.; Lv, Y.; Sun, Y.; Zhu, Y. Performance enhancement of ZnO photocatalyst via synergic effect of surface oxygen defect and graphene hybridization. *Langmuir* **2013**, *29*, 3097–3105. [\[CrossRef\]](#)
19. Leung, Y.; Chen, X.; Ng, A.; Guo, M.; Liu, F.; Djuricic, A.; Chan, W.; Shi, X.; Van Hove, M. Green emission in ZnO nanostructures—Examination of the roles of oxygen and zinc vacancies. *Appl. Surf. Sci.* **2013**, *271*, 202–209. [\[CrossRef\]](#)
20. Kusiak-Nejman, E.; Wojnarowicz, J.; Morawski, A.W.; Narkiewicz, U.; Sobczak, K.; Gierlotka, S.; Lojkowski, W. Size-dependent effects of ZnO nanoparticles on the photocatalytic degradation of phenol in a water solution. *Appl. Surf. Sci.* **2021**, *541*, 148416. [\[CrossRef\]](#)
21. Pimentel, A.; Ferreira, S.H.; Nunes, D.; Calmeiro, T.; Martins, R.; Fortunato, E. Microwave Synthesized ZnO Nanorod Arrays for UV Sensors: A Seed Layer Annealing Temperature Study. *Materials* **2016**, *9*, 299. [\[CrossRef\]](#)
22. Samadipakchin, P.; Mortaheb, H.R.; Zolfaghari, A. ZnO nanotubes: Preparation and photocatalytic performance evaluation. *J. Photochem. Photobiol. A Chem.* **2017**, *337*, 91. [\[CrossRef\]](#)
23. Zhang, Y.; Ram, M.K.; Stefanakos, E.K.; Goswami, Y.D. Synthesis, Characterization, and Applications of ZnO Nanowires. *J. Nanomater.* **2012**, *12*, 624520. [\[CrossRef\]](#)
24. Diguna, L.J.; Fitriani, A.D.; Liasari, B.R.; Timuda, G.E.; Widayatno, W.B.; Wismogroho, A.S.; Zeng, S.; Birowosuto, M.D.; Amal, M.I. Optical and Photodetection Properties of ZnO Nanoparticles Recovered from Zn Dross. *Crystals* **2021**, *11*, 6. [\[CrossRef\]](#)
25. Borysiewicz, M.A. ZnO as a Functional Material, a Review. *Crystals* **2019**, *9*, 505. [\[CrossRef\]](#)
26. Zhong, J.B.; Li, J.Z.; He, X.Y.; Zeng, J.; Lu, Y.; Hu, W.; Lin, K. Improved Photocatalytic Performance of Pd-Doped ZnO. *Curr. Appl. Phys.* **2012**, *12*, 998–1001. [\[CrossRef\]](#)
27. Sin, J.; Lam, S.; Lee, K.; Mohamed, A. Preparation and photocatalytic properties of visible light-driven samarium-doped ZnO nanorods. *Ceram. Int.* **2013**, *39*, 5833–5843. [\[CrossRef\]](#)
28. Ahmad, M.; Ahmed, E.; Zhang, Y.; Khalid, N.R.; Xu, J.; Ullah, M.; Hong, Z. Preparation of Highly Efficient Al-Doped ZnO Photocatalyst by Combustion Synthesis. *Curr. Appl. Phys.* **2013**, *13*, 697–704. [\[CrossRef\]](#)
29. Huang, L.; Ren, N.; Li, B.; Zhou, M. Effect of Annealing on the Morphology, Structure and Photoelectric Properties of AZO/Pt/FTO Trilayer Films. *Acta Metall. Sin. Engl. Lett.* **2015**, *28*, 281–288. [\[CrossRef\]](#)
30. Haja sheriff, M.H.; Murugan, S.; Manivasaham, A.; Ashok Kumar, R. Electro spray technique to enhance the physical property of Sulphur doped zinc oxide thin film. *Mater. Today Proc.* **2021**, *47*, 1717–1723. [\[CrossRef\]](#)
31. Riaz, A.; Ashraf, A.; Taimoor, H.; Javed, S.; Akram, M.A.; Islam, M.; Mujahid, M.; Ahmad, I.; Saeed, K. Photocatalytic and Photostability Behavior of Ag- and/or Al- Doped ZnO Films in Methylene Blue and Rhodamine B Under UV-C Irradiation. *Coatings* **2019**, *9*, 202. [\[CrossRef\]](#)
32. Lavand, A.B.; Malghe, Y.S. Synthesis, characterization and visible light photocatalytic activity of nitrogen-doped zinc oxide nanospheres. *J. Asian Ceram. Soc.* **2018**, *3*, 305–310. [\[CrossRef\]](#)
33. Hamrouni, S.; AlKhalifah, M.S.; El-Bana, M.S.; Zobaidi, S.K.; Belgacem, S. Deposition and characterization of spin-coated n-type ZnO thin film for potential window layer of solar cell. *Appl. Phys. A* **2018**, *124*, 555. [\[CrossRef\]](#)
34. Farrag, A.A.-G.; Balboul, M.R. Nano ZnO thin films synthesis by sol-gel spin coating method as a transparent layer for solar cell applications. *J. Sol-Gel Sci. Technol.* **2016**, *82*, 269–279. [\[CrossRef\]](#)
35. Yan, X.; Venkataraj, S.; Aberle, A.G. Wet-Chemical Surface Texturing of Sputter-Deposited ZnO: Al Films as Front Electrode for Thin-Film Silicon Solar Cells. *Int. J. Photoenergy* **2015**, *2015*, 1–10. [\[CrossRef\]](#)
36. Islam, M.R.; Rahman, M.; Farhad, S.F.U.; Podder, J. Structural, optical and photocatalysis properties of sol-gel deposited Al-doped ZnO thin films. *Surf. Interfaces* **2019**, *16*, 120–126. [\[CrossRef\]](#)
37. Mahdavi, R.; Talesh, S.S.A. Sol-gel synthesis, structural and enhanced photocatalytic performance of Al doped ZnO nanoparticles. *Adv. Powder Technol.* **2017**, *28*, 1418–1425. [\[CrossRef\]](#)
38. Aydın, C.; AbdEl-sadek, M.S.; Zheng, K.; Yahia, I.S.; Yakuphanoglu, F. Synthesis, diffused reflectance and electrical properties of nanocrystalline Fe-doped ZnO via sol-gel calcination technique. *Opt. Laser Technol.* **2013**, *48*, 447–452. [\[CrossRef\]](#)
39. Ravichandran, K.; Sindhuja, E.; Uma, R.; Arun, T. Photocatalytic efficacy of ZnO films light intensity and thickness effects. *Surf. Eng.* **2017**, *33*, 512–520. [\[CrossRef\]](#)
40. Nassar, M.Y.; Mohamed, T.Y.; Ahmed, I.S.; Mohamed, N.M.; Khatab, M. Hydrothermally Synthesized Co₃O₄, α-Fe₂O₃, and CoFe₂O₄ Nanostructures: Efficient Nano-adsorbents for the Removal of Orange G Textile Dye from Aqueous Media. *J. Inorg. Organomet. Polym. Mater.* **2017**, *27*, 1526–1537. [\[CrossRef\]](#)
41. Thomas, B.; Alexander, L.K. Enhanced synergetic effect of Cr(VI) ion removal and anionic dye degradation with superparamagnetic cobalt ferrite meso-macroporous nanospheres. *Appl. Nanoscience* **2018**, *8*, 125–135. [\[CrossRef\]](#)
42. Hassani, A.; Eghbali, P.; Ekicibil, A.; Metin, Ö. Monodisperse cobalt ferrite nanoparticles assembled on mesoporous graphitic carbon nitride (CoFe₂O₄/mpg-C₃N₄): A magnetically recoverable nanocomposite for the photocatalytic degradation of organic dyes. *J. Magn. Magn. Mater.* **2018**, *456*, 400–412. [\[CrossRef\]](#)
43. Parhizkar, J.; Habibi, M. Hossein Investigation and Comparison of Cobalt ferrite composite nanoparticles with individual Iron oxide and Cobalt oxide nanoparticles in azo dyes removal. *J. Water Environ. Nanotechnol.* **2019**, *4*, 17–30.

-
44. Saber, O.; El-Brolossy, T.A.; Al Jaafari, A.A. Improvement of Photocatalytic Degradation of Naphthol Green B Under Solar Light Using Aluminum Doping of Zinc Oxide Nanoparticles. *Water Air Soil Pollut.* **2012**, *223*, 4615–4627. [[CrossRef](#)]
 45. Wolf, P.A. Theory of the band structure of very degenerate semiconductors. *Phys. Rev.* **1962**, *126*, 405. [[CrossRef](#)]
 46. Singh, A.P.; Kumari, S.; Shrivastav, R.; Dass, S.; Satsangi, V.R. Iron doped nanostructured TiO₂ for photoelectrochemical generation of hydrogen. *Int. J. Hydrog. Energy* **2008**, *33*, 5363–5368. [[CrossRef](#)]